Available online at website: https://journal.bcrec.id/index.php/bcrec

Bulletin of Chemical Reaction Engineering & Catalysis, 21 (3) 2026, 526-538

Original Research Article

Enhanced Photocatalytic Activity of Bi_3NbO_7 by Fabrication of $CuBi_2O_4/Bi_3NbO_7$ Heterojunction Photocatalyst

Zhenkun Cheng, Dongbin Liu, Lihui Fan, Yanming Shen*

Department of Chemical Engineering, Shenyang University of Chemical Technology, Shenyang 110142, China.

Received: 13th February 2026; Revised: 18th March 2026; Accepted: 20th March 2026
Available online: 23th March 2026; Published regularly: October 2026

Abstract

Bi_3NbO_7 has been widely studied as a bismuth-based photocatalyst for degradation of organic pollutants. However, the fast recombination of photo-excited carriers limits its photocatalytic performance. In this work, the $CuBi_2O_4/Bi_3NbO_7$ heterojunction was successfully fabricated, and its photocatalytic performance was evaluated by degradation of TC under stimulated sunlight. The optimal TC degradation efficiency of 85% was obtained on $CuBi_2O_4/Bi_3NbO_7$ heterojunction with $CuBi_2O_4$ mass ratio of 10% at the condition as initial TC concentration of 40 mg/L and photocatalyst dosage of 1 g/L. This optimal TC degradation efficiency is greatly higher than that of bulk Bi_3NbO_7 with the reaction rate constant reached 0.035 min^{-1} which is 3.7 times as that of Bi_3NbO_7. The photocatalytic degradation mechanism that based on type-II heterojunction was proposed. This work provided a promising strategy to design highly efficient photocatalysts for environmental remediation.

Keywords: Bi-based semiconductor; Bi_3NbO_7; Heterojunction; dye degradation; photocatalysis

How to Cite: Cheng, Z., Liu, D., Fan, L., Shen, Y. (2026). Enhanced Photocatalytic Activity of Bi_3NbO_7 by Fabrication of $CuBi_2O_4/Bi_3NbO_7$ Heterojunction Photocatalyst. *Bulletin of Chemical Reaction Engineering & Catalysis*, 21 (3), 526-538. (DOI: 10.9767/bcrec.20670)

Permalink/DOI: https://doi.org/10.9767/bcrec.20670

1. Introduction

Nowadays, the use of antibiotics has greatly increased in both human and animal healthcare to control the spread of diseases. These antibiotics cannot be completely absorbed by the body and the unabsorbed portion being excreted and subsequently entering the environment, where it may persist, posing significant risks to ecosystem [1,2]. Tetracycline is one of the most commonly used antibiotics for treating microbial infections in both human and animals. However, after medication, about 75% of TC enters the ecosystem in its active form through urine and feces [3]. Various methods have been explored to remove TC from wastewater, such as adsorption, biodegradation, membrane separation, coagulant sedimentation, advanced oxidation processes (AOPs) and so on [4-6]. Photocatalysis technology, which is belonged to one of AOPs, is widely employed to oxidize antibiotics into molecules that are easily biodegradable, less hazardous, and even harmless due to which it has received much concern from scientists [7]. The development of an efficient photocatalyst is crucial to photocatalytic degradation of pollutants. In the recent years, bismuth-based semiconductors have emerged as highly promising materials in photocatalysis, particularly due to their efficiency in harnessing visible light [8]. Various types of bismuth-based semiconductors have been developed, including Bi_2O_3, Bi_2WO_6, Bi_2MoO_6, $BiVO_4$, $Bi_2O_2CO_3$, Bi_3NbO_7, BiO_X (X = Cl, Br, I), etc [9-13]. Majority of bismuth-based semiconductors possess narrow bandgap less than 3.0 eV, originated from the valence band consists of Bi 6s and O 2p hybrid orbitals [14,15]. However, there are still exist limitations in practice of these semiconductors.

---

* Corresponding Author.
Email: sym6821@sina.com.cn (Y.-M. Shen)

For example, the valence band (VB) potential or the conduction band (CB) potential of bismuth-based semiconductors is not positive or negative enough to produce the photo-excited holes or electrons with sufficient redox ability to drive the specific photocatalytic reactions, for example to produce free radicals including hydroxyl radical ($\bullet OH$) and superoxide radical ($\bullet O_2^-$), which is crucial for photocatalytic pollutant removal[16]. Secondly, the excited electrons recombine with holes more easily and quickly in narrow-bandgap semiconductors [16]. Bi_3NbO_7 is one kind of bismuth-based semiconductors with oxygen-deficient fluorite structure, and possesses excellent electrical and optical properties [17-21]. Nevertheless, its photocatalytic ability is limited by the poor separation of the photo-excited carriers [22,23]. An effective strategy for improvement of the photocatalytic activity of Bi_3NbO_7 was the construction of a heterojunction with other semiconductors. The reported semiconductors used for this purpose included $BiOIO_3$, $Bi_2C_2CO_3$, CuO, Bi_2MoO_6, BiOCl, g-C_3N_4, $LaFeO_3$, Bi_2O_3 and so on [22-30].

Copper bismuthate ($CuBi_2O_4$) has recently gained attention as a visible-light responsive *p*-type semiconductor photocatalyst, due to its favorable band position, narrow band gap (1.5-1.8 eV), visible light absorption, low cost, and high flat band potential. However, $CuBi_2O_4$ suffers from a low absorption coefficient, high charge recombination rate, and poor charge transport, stemming from its electronic band structure [31,32]. These limitations restrict the applications of $CuBi_2O_4$. The conduction band (CB) of $CuBi_2O_4$ is highly negative, facilitating the reduction reactions. At the same time, the valence band (VB) of $CuBi_2O_4$ possesses so higher position that aligns with the conduction bands of different semiconductors, making it a candidate with great potential in the formation of heterojunction systems aimed at modifying redox potentials at interfacial regions [33]. Considering the band structures of Bi_3NbO_7 and $CuBi_2O_4$, in this work, we used $CuBi_2O_4$ to modify Bi_3NbO_7 by fabrication of $CuBi_2O_4/Bi_3NbO_7$ heterojunction photocatalyst, aiming at improving the photocatalytic activity of Bi_3NbO_7. The photocatalytic activity was evaluated by degradation of TC. The effect of $CuBi_2O_4/Bi_3NbO_7$ ratio on the photocatalytic performance was investigated. Moreover, a possible mechanism for degradation of TC by $CuBi_2O_4/Bi_3NbO_7$ heterojunction photocatalyst was proposed.

2. Materials and Method

2.1 Preparation of Photocatalyst

Bi_3NbO_7 was prepared according to the method described elsewhere [34,24]. Typically, 0.5 g of Nb_2O_5 was dispersed in 3 mL of HF solution (17 wt%), then the resulting suspension was transferred to an autoclave and heated at 150 °C for 4 h, forming a clear solution A. 5.48 g of $Bi(NO_3)_3 \cdot 5H_2O$ was dissolved into 50 mL of HNO_3 (4 mol/L) under stirring, resulting a clear solution B. Both of solution A and B were dropped into 10 mL of KOH solution (4 mol/L), keeping the pH around 13 by simultaneously dropping KOH solution (4 mol/L). After stirring for 2 h, the suspension was centrifugally separated, and the wet product was washed repeatedly with distillated water and anhydrous ethanol, respectively, until the solution reached neutrality. After centrifugally separation, the wet solid powder was vacuum dried at 60 °C, resulting in the precursor of Bi_3NbO_7 which was subsequently heated at 500 °C for 8 h to obtain the faint yellow Bi_3NbO_7 powder, which was noted as BNO.

$CuBi_2O_4$ was synthesized by hydrothermal method. Typically, 5.48 g of $Bi(NO_3)_3 \cdot 5H_2O$ and 1.21 g of $Cu(NO_3)_2 \cdot 3H_2O$ were dissolved into 50 mL of HNO_3 (4 mol/L). After stirring for 30 min, the pH of the solution was adjusted to 13 by adding KOH solution (4 mol/L). The solution was stirred for 3 h to obtain the precursor. The resulting precursor was transferred into a Teflon autoclave and heated at 180 °C for 24 h. Subsequently, the resulted solid particles were collected by centrifugation and then washed several times with distilled water and absolute ethanol, and finally dried at 80 °C for 6 h to form $CuBi_2O_4$ nanoparticles, which was labelled as CBO.

$CuBi_2O_4/Bi_3NbO_7$ composite photocatalysts were fabricated by an impregnation method. The weighted as-prepared $CuBi_2O_4$ and Bi_3NbO_7 powders were diapered in 25 mL of methanol under ultrasonication for 30 min, respectively. Then, the resulted two solutions were mixed together and stirred for 3 h. Subsequently, the suspension was heated at 60 °C until the methanol was completely evaporated. The collected solid was heated at 300 °C for 2 h. Finally, the $CuBi_2O_4/Bi_3NbO_7$ composites were obtained, and labelled as CBO/BNO-*x*, where *x* refers to the $CuBi_2O_4/Bi_3NbO_7$ mass ratio. Figure 1 shows the schematic diagram for the preparation of the CBO/BNO composite.

2.2 Characterizations

The phases of the resultant sample was analyzed by X-ray diffraction (XRD) using a Bruker D8 ADVANCE diffractometer under CuKα radiation (λ=0.15406 nm), operating at 40 KV and 40 mA over the 2θ range from 10 to 70°. The morphology and microstructure of the as-obtained sample were observed through a scanning electron microscope (SEM, ZEISS Gemini SEM 300) and a transmission electron microscope (FEI Titan G2 60-300), respectively. UV-vis diffuse reflectance spectra were recorded on a UV-vis spectrophotometer (UV-3600, Shimadzu) equipped with an integrating sphere, and BaSO4 was used as the reference. X-ray photoelectron spectroscopy (XPS) data were captured on an XPS photoelectron spectrometer (ESCALAB250, Thermo Fisher) equipped with the Mg Kα achromatic X-ray source. The specific surface area and pore structure of the samples were evaluated by the nitrogen adsorption-desorption isotherms measured by a physiochemical adsorption instrument (V-Sorb 2800P, Beijing APP Co. Ltd, China). The content of total organic carbon (TOC) of the solutions were obtained using a TOC analyzer (TOC-L CPH, Shimadzu Corp., Japan). Free radicals formed by the samples under irradiation were detected through the EPR technique (Bruker Magnettech ESR5000). 5,5-dimethyl-1-pyrrolin-n-oxide (DMPO) was used as the trapping agent for hydroxyl and superoxide, and methanol was used as the reaction solvent, while and 2,2,6,6-Tetramethylpiperidoxyl (TEMPO) was used as the trapping agent for holes and water was used as the reaction solvent. The electrochemical performance was analyzed by the Mott-Schottky spectroscopy (MS), electrochemical impedance spectroscopy (EIS) and photocurrent response measurements using an electrochemical workstation (CHI 660E, Shanghai CH Instruments Co., China) with a three-electrode system, where Pt plate was used as the contrast electrode and Ag/AgCl as the reference electrode. The working electrode was prepared by coating the as-prepared material on an indium tin oxide (ITO) conductive glass and drying at 60 °C for 1 h. $K_3[Fe(CN)_6]$-$K_4[Fe(CN)_6]$-KCl solution (10 mmol/L) was used as the supporting electrolyte solution.

2.3 Photocatalytic Activity Measurements

A 300 W Xenon lamp was used as the irradiation source. The lamp was located on the top of the solution with the distance of 10 mm. The as-prepared photocatalyst was dispersed into a jacketed beaker containing 100 ml TC solution according to the predetermined dosage. The degradation reaction was performed at 25 °C kept by the circulating water from a water bath. After regular intervals, the samples were taken and filtrated by a 0.22 μm filter membrane to separate the photocatalyst for analysis. The TC concentration was measured by a spectrophotometer at wavelength of 356 nm. The TC degradation efficiency (η%) was calculated as follows:

$$\eta\% = \frac{C_0 - C}{C_0} \times 100\% \qquad (1)$$

where C_0 (mg/L) and C (mg/L) refer to TC concentration at the starting and reaction time t, respectively.

3 Results and Discussion

3.1 Characterizations

Figure 2 provides the XRD patterns of Bi_3NbO_7, $CuBi_2O_4$, and $CuBi_2O_4/Bi_3NbO_7$ composites. The pristine Bi_3NbO_7 exhibits distinct diffraction peaks at 2θ angles of 28.2°, 32.7°, 46.8°, 55.7° and 58.5°, corresponding to the crystal planes (111), (200), (220), (311) and (222), of Bi_3NbO_7 (JCPDS No.86-0875). The pristine $Cu_2Bi_2O_4$ presents the diffraction peaks located at 2θ angles of 20.8°, 28.0°, 30.7°, 33.3°, 37.4°, 46.7°, 52.9° and 55.6°, matching with the crystal planes (200), (211), (002), (310), (202), (411), (213) and

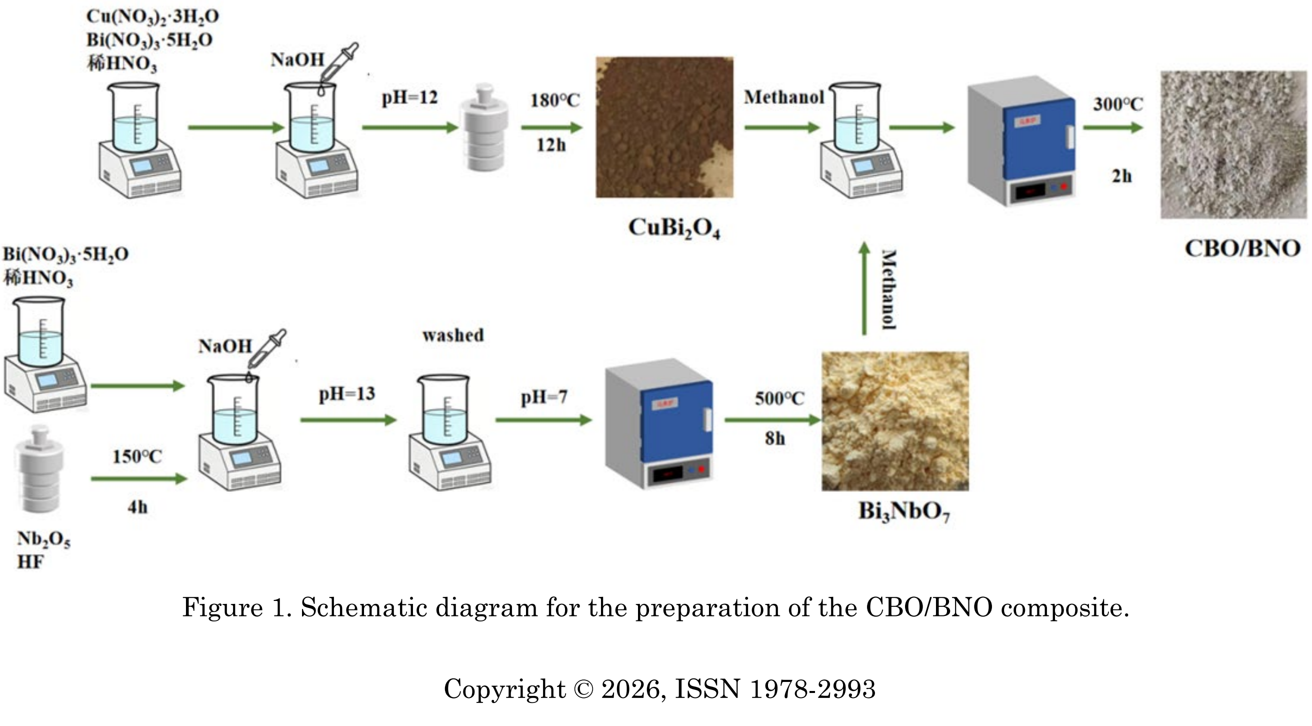

Figure 1. Schematic diagram for the preparation of the CBO/BNO composite.

(332) of $Cu_2Bi_2O_4$ (JCPDS No.86-0875). In the patterns of $CuBi_2O_4/Bi_3NbO_7$ composites, there emerge clear diffraction peaks of Bi_3NbO_7, but no clear diffraction peaks of $CuBi_2O_4$, due to the lower combination amounts of $CuBi_2O_4$. In the local magnification patterns, the diffraction peaks (2θ angles of 20.8° and 37.4°) of $CuBi_2O_4$ can be observed, and the intensities increase with the increase in $CuBi_2O_4$ combination amount, indicating the successful preparation of $CuBi_2O_4/Bi_3NbO_7$ composites.

The morphology of Bi_3NbO_7, $CuBi_2O_4$, and $CuBi_2O_4/Bi_3NbO_7$ composites was studied by SEM and TEM. As shown in Figure 3a, the pristine $CuBi_2O_4$ exhibit nanocolumn-shaped particles that self-assembled into microspheres, with an estimated mean diameter of 2-3 μm [35]. The pristine Bi_3NbO_7 presents agglomerated nanoparticles (Figure 3b). The CBO/BNO composite exhibits the hybrid morphology of $CuBi_2O_4$ and Bi_3NbO_7, which contains CBO microspheres with smaller BNO nanoparticles

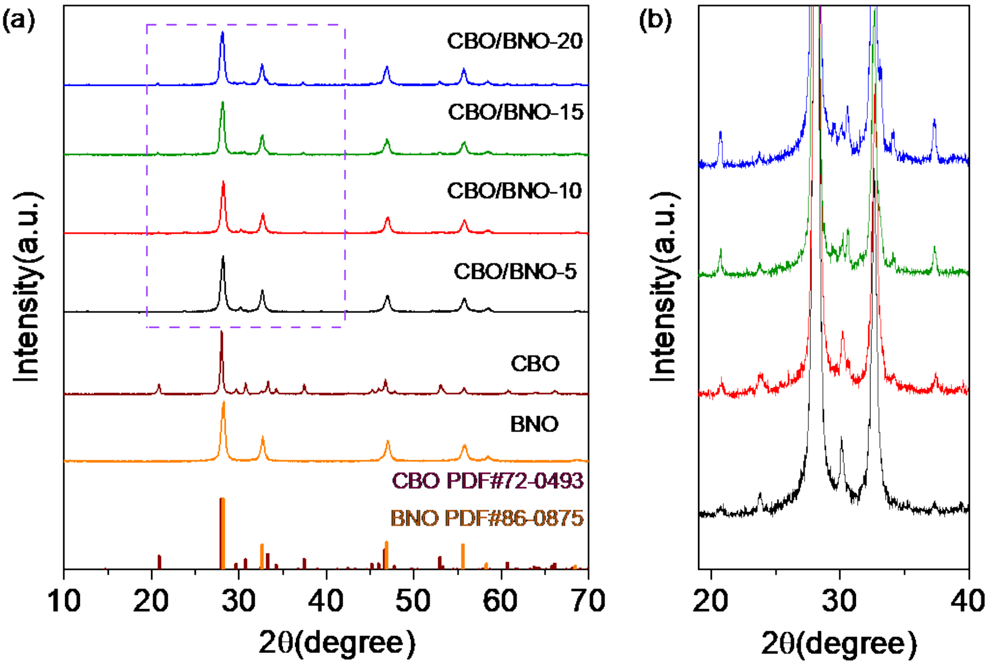

Figure 2. XRD patterns of Bi_3NbO_7, $CuBi_2O_4$, and CBO/BNO composites (a) and (b) local magnification patterns of CBO/BNO composites..

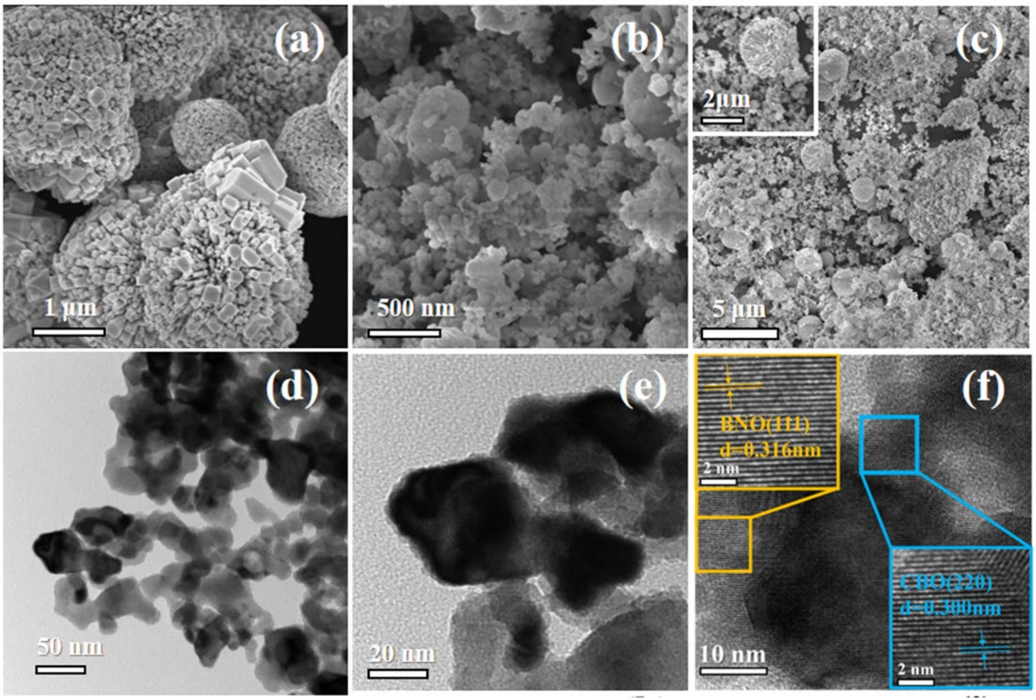

Figure 3. SEM images of (a) $CuBi_2O_4$, (b) Bi_3NbO_7, (c) $CuBi_2O_4/Bi_3NbO_7$, (d-f) TEM images of CBO/BNO-10.

distributed over its surface. TEM images show the CBO/BNO composite presents the agglomerated nanoparticles shape. HRTEM image indicates the distinct lattice fringes of CBO and BNO, with the measured lattice spacing of 0.316 nm and 0.3 nm, corresponding to the plane (111) of Bi_3NbO_7 and the (220) plane of $CuBi_2O_4$, respectively. The EDX result (Figure S1a) confirmed the presence of characteristic peaks corresponding to Cu, Bi, Nb, and O elements. Elemental mapping results (Figure S1b) reveal that these constituent elements distribute uniformly on the surface. The results of morphology analysis illustrate the successful fabrication of $CuBi_2O_4/Bi_3NbO_7$ heterojunction, which is agreement with the results of XRD.

Figure 4 provides the N_2 adsorption–desorption isotherms and the pore size distribution curves for CBO, BNO, and CBO/BNO composites. As shown in Figure 4a, the isotherms of all samples are associated to type IV with a distinct H3-type hysteresis loop, indicating the presence of mesoporous pores. As listed in table S1, the BET specific surface area of CBO is determined as 4.25 m^2/g, while that of Bi_3NbO_7 is 14.48 m^2/g. In comparison, the specific surface area is ~3.4 folds of that of CBO. This is originated from that BNO possesses the loose agglomerated nanoparticle structure, while CBO exhibited compact microsphere structure, as illustrated in SEM images. The specific surface area of CBO/BNO composites displays an increase trend with the increase in the combination amount of BNO, except CBO/BNO-10. As shown in Figure 4b, the pore size distributions curves indicate that the pores in all samples mainly exist in form of mesoporous pores, accompanied by macroporous pores.

XPS analysis was performed to investigate the surface composition and chemical state of $CuBi_2O_4$, Bi_3NbO_7, and $CuBi_2O_4/Bi_3NbO_7$ composite. Figure 5 shows the high-resolution XPS spectra of Bi 4f, Nb 3d, Cu 2p, and O 1s. As shown in Figure 5a, the Bi 4f spectra present two peaks at 163.7~164.0 and 158.3~158.7 eV which are assigned to Bi $4f_{5/2}$ and Bi $4f_{7/2}$, respectively, indicating that the existence of Bi^{3+} in the samples [24,17]. Compared with those of BNO and CBO, the Bi 4f binding energy of CBO/BNO-10 shifts to higher energy position. The spectra of Nb 3d of BNO and CBO emerge two distinct peaks located at 209.0 and 206.2 eV, corresponding to Nb $3d_{3/2}$ and Nb $3d_{5/2}$, revealing that Nb exists in the valence state of Nb^{5+}. The binding energy of Nb 3d shows almost no change after combination of BNO with CBO. It can be seen from Figure 5c, in the Cu 2p spectrum of CBO, the peaks at 953.1 and 933.3 eV belong to the Cu $2p_{1/2}$ and Cu $2p_{3/2}$, respectively. The peaks at 941.5 eV and the peak at 961.6 eV are satellite peaks of Cu^{2+}. These peaks are the characteristic peaks of Cu^{2+} [35-37]. In the Cu 2p spectrum of CBO/BNO-10, the characteristic peaks shifted to lower binding energy positions at 932.3 and 952.1 eV, accompanied by the shift of the satellite peaks to lower energy positions at 940.1 and 959.9 eV, respectively. The shifts in binding energies of Bi 4f and Cu 2p indicate that the changes in the electron cloud density due to the movement of electrons from BNO to CBO during the formation of the composite [36]. The O 1s peak in the spectrum of BNO was fitted to three peaks at 529.3 eV, 531.7 eV and 533.4 eV, respectively, corresponding to Bi-O bond, Nb-O and oxygen in hydrated species OH on the surface, respectively [17]. The O 1s in the spectrum of CBO exhibits two fitted peaks at 529.0 eV and 530.6 eV, which are associated to lattice oxygen from Bi-O bond and oxygen vacancy, respectively [38,39]. The O 1s binding energy of CBO/BNO-10 is located between those of bulk CBO and BNO, indicating heterojunction formation.

The band gaps (E_g) of CBO, BNO and the CBO/BNO composites were determined by UV-vis DRS tests. As shown in Figure 6a, the bulk Bi_3NbO_7 shows an intensive absorption peak with absorption edge at range of 400-600 nm. The bulk $CuBi_2O_4$ exhibits a broad absorption peak with

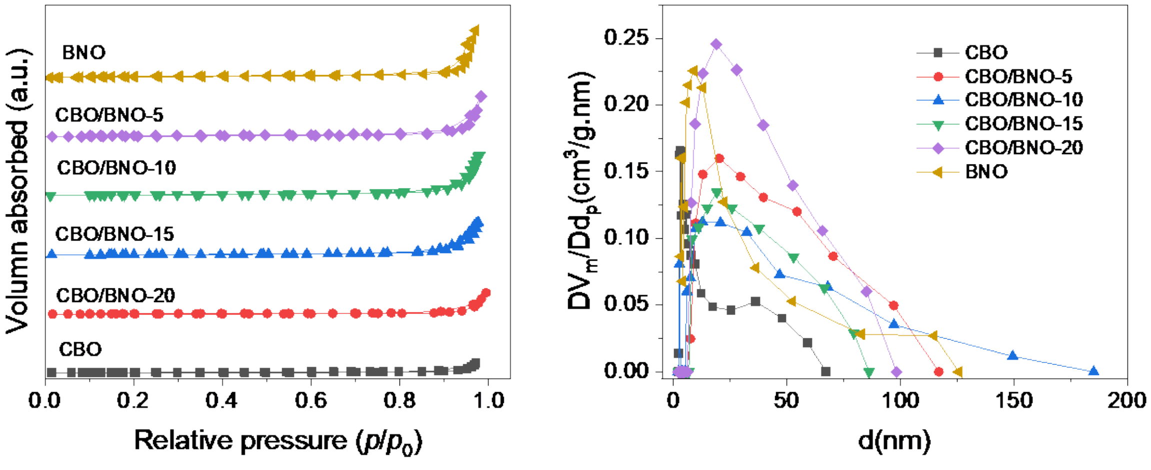

Figure 4. (a) N_2 adsorption-desorption isotherms and (b) pore size distribution curves of samples.

absorption edge between 620-800 nm. For the CBO/BNO composites, the absorption curves present the hybrid absorption of CBO and BNO, displaying the formation of a heterojunction [40]. The band gaps of the samples were further estimated using Kubelka-Munk formula (Equation 2):

$$\alpha h\nu = A(h\nu - E_g)^{n/2} \tag{2}$$

Here, α, h, v, A and E_g represent the absorption coefficient, Planck constant, light frequency, proportion constant and band gap, respectively. The value of n is related to the type of semiconductor, n =1 for the direct semiconductor, whereas n = 4 for an indirect semiconductor. CBO and BNO are belonged to direct and indirect semiconductor, respectively. Therefore, based on the plot of $(\alpha h\nu)^2/(\alpha h\nu)^{1/2}$ versus $h\nu$. The band gaps were estimated to be 1.72 eV and 2.2 eV for CBO and BNO, respectively.

To determine the energy band positions of CBO and BNO, the Mott-Schottky (M-S) curves were studied. As shown in Figure 6(c-d), the positive slope of M-S curve indicate BNO is a *n*-type semiconductor, whereas the negative slope reveals CBO is a *p*-type semiconductor. The estimated flat-band potentials were -0.48 V and 0.75 V (*vs* Ag/AgCl) for BNO and CBO, respectively. According to the equation (E_{NHE} = $E_{\mathrm{Ag/AgCl}}$ + 0.197) [23,26], the resulted flat-band potentials were converted to standard hydrogen electrode (NHE) potentials of -0.28 V and 0.95 V. Considering that the flat-band potential is 0.2 eV higher than the potential of the conduction band (CB) for the *n*-type semiconductors [36], whereas 0.1 eV lower than the potential of the valence band (VB) [40], the CB of BNO and the VB of CBO were estimated to be -0.48 eV and 1.05 eV, respectively. According to the equation, $E_{\mathrm{VB}} = E_{\mathrm{CB}} + E_{\mathrm{g}}$, the VB of BNO and CB of CBO potentials were calculated to be 1.72 and 0.67 eV for BNO and CBO, respectively. The VB potentials of CBO and BNO were also investigated by XPS valence tests. As shown in Figure 6(e-f), the VB potentials of CBO and BNO were determined as 1.69 and 1.03 eV, respectively, which are agreement with those obtained by M-S tests.

The interface charge transport behavior of the samples was studied by electrochemical impedance spectroscopy (EIS) measurements. The arc radius of the Nyquist plot was used to evaluate the charge transfer resistance at the material surface. The smaller arc radius indicates faster charge transfer and more effective photo-excited charge carrier separation [40]. As shown in Figure 7a, among these photocatalysts, sample CBO/BNO-10 exhibits the smallest arc radius the smallest radius, indicating the lowest resistance and the highest charge carrier separation efficiency during the transfer of charges. The photocurrent response and carrier transfer under

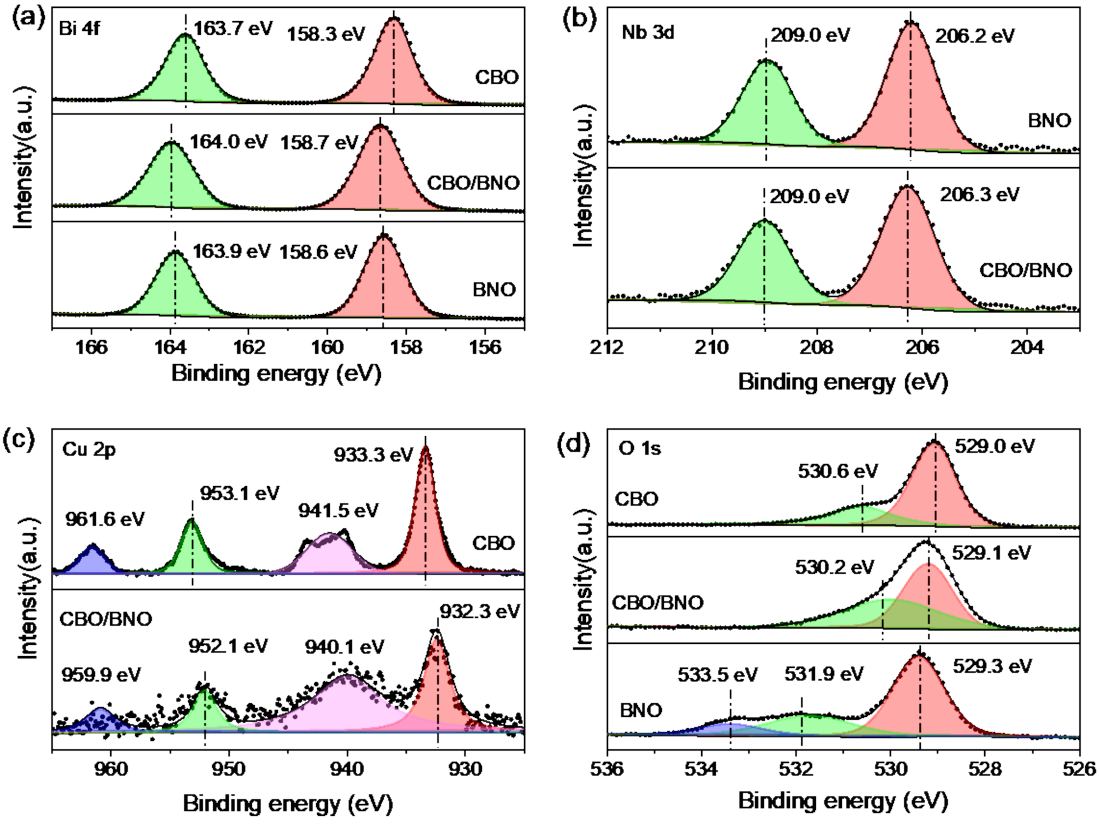

Figure 5. XPS spectra of (a) Bi 4f, (b) Nb 3d, (c) Cu 2p and (d) O 1s.

irradiation of stimulated sunlight was further investigated by photoelectrochemical measurement. As shown in Figure 7b, the highest photocurrent density was observed for CBO/BNO-10, implying the highest photocurrent response among these samples, which is agreement with the results of EIS test.

3.2 Photocatalytic Performance

The photocatalytic performance of photocatalysts were evaluated by degradation of TC under irradiation of stimulated sunlight. It can be seen from Figure 8a, after irradiation of 60 minutes, the *C*/*C*₀ decreased from 1 to 0.67 and 0.49 on CBO and BNO, corresponding to TC degradation efficiencies of 33% and 51%, respectively. For the CBO/BNO composites, the *C*/*C*₀ greatly declined to 0.24, 0.15, 0.20 and 0.25, which is associated to the TC degradation efficiencies of 76%, 85%, 80% and 75%, on composites CBO/BNO-5, CBO/BNO-10, CBO/BNO-15 and CBO/BNO-20, respectively, revealing that the CBO/BNO heterojunction presents the higher photocatalytic activity than bulk CBO and BNO. Moreover, the highest TC degradation efficiency was found on CBO/BNO-10, implying that an appropriate combination amount of CBO and BNO is necessary to effectively improve the photocatalytic activity of bulk BNO. Generally, the photocatalytic degradation of the pollutant in solution by the solid photocatalyst involves three consecutive

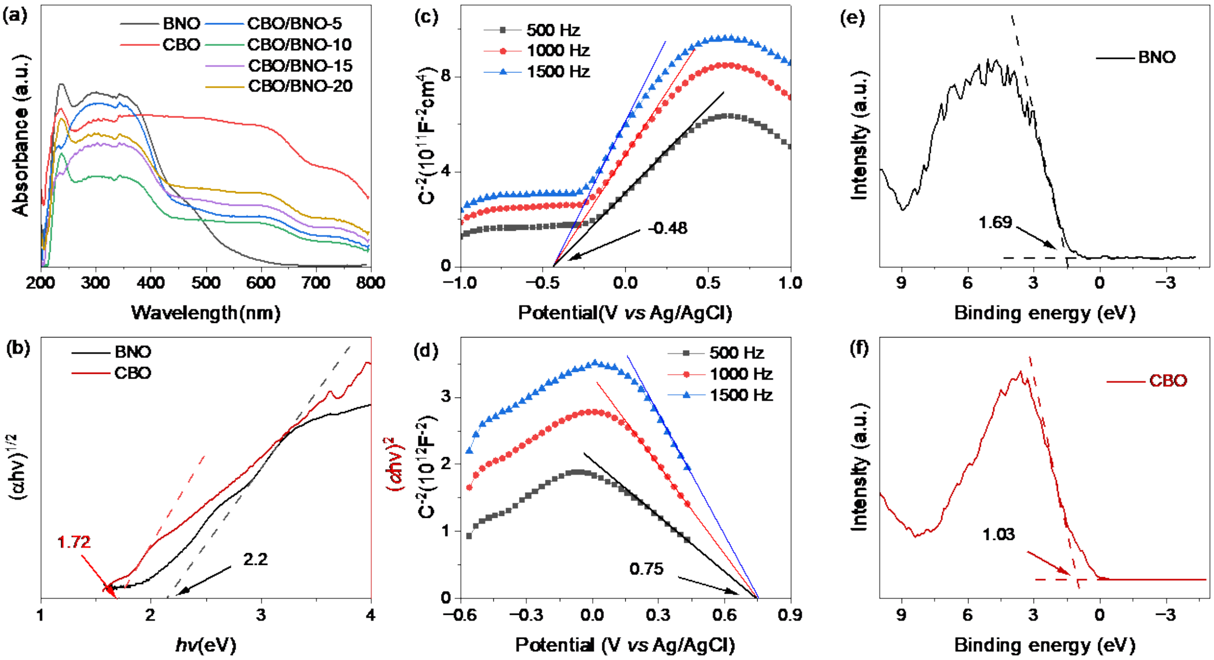

Figure 6. (a) UV-vis DRS spectra and (b) Tauc plots of photocatalysts; Mott-Schottky curves of (c) Bi_3NbO_7 and (d) $CuBi_2O_4$; VB-XPS spectra of (e) Bi_3NbO_7 and (f) $CuBi_2O_4$.

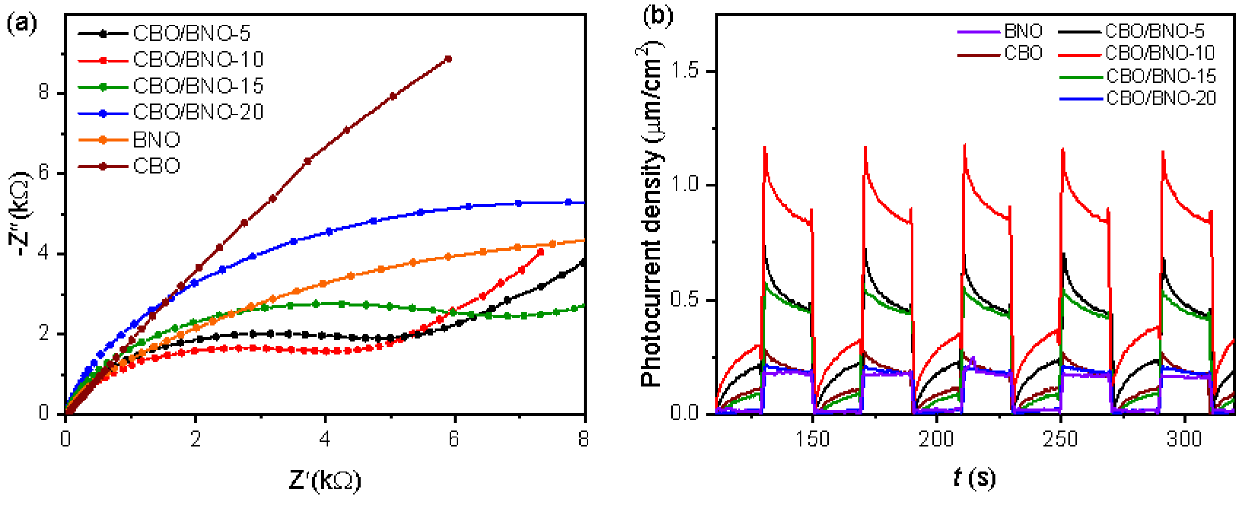

Figure 7. (a) EIS plots and (b) Photocurrent response of photocatalysts.

steps: the adsorption of the pollutant onto the surfaces of the solid photocatalyst, the photocatalytic degradation of the adsorbed pollutant, and the desorption of the degraded products from the surfaces of the photocatalyst. As shown in Figure 8, the adsorption process displays weaker contribution on the TC degradation, as compared to the photocatalytic degradation. Although the specific area of CBO/BNO-10 is lower than those of other CBO/BNO heterojunction photocatalysts, the optimal TC degradation efficiency was obtained on CBO/BNO-10. This is originated from the efficient separation of photo-excited carriers on the CBO/BNO-10 heterojunction photocatalyst, as evidenced by the results of EIS and photocurrent response tests (see Figure 7). The first-order kinetics model was used to fit the photocatalytic degradation data. The results display that the photocatalytic degradation of TC follows better first-order kinetics due to the higher correlation coefficients as above 0.96 (see Table S2). The optimal reaction rate constant k of 0.035 min^{-1} was found on CBO/BNO-10 photocatalyst, which is 3.7 times as that on bulk BNO.

Figure 8c provides the UV-vis scanning curves of the TC solution during the photocatalytic degradation process. As shown in Figure 8c, two distinct absorption peaks centered at 275 and 356 nm emerge in the TC spectrum. As illustrated in Figure S2, the peak at 275 nm was reported to be related to the structure of aromatic ring A, which includes enolic hydroxyl, amide, and ketone groups, whereas the peak at 357 nm was attributed to aromatic rings B, C, and D [41]. As the photocatalytic degradation proceeded, the intensities of the two peaks gradually declined, indicating that TC was destroyed in structure and decomposed to intermediates, even mineralized into CO_2 and H_2O. It is also found that the peak at 275 nm still exhibited a relative higher intensity after irradiation of 60 min, implying the incomplete decomposition of TC and forming some intermediates. To further find out the change of TC during the degradation process, TOC analysis was conducted. As shown in Figure 8d, as the photocatalytic degradation proceeded, the TOC/TOC_0 value decreased, displaying the decrease in concentration of organic compounds. However, the value of TOC/TOC_0 is not zero and higher than that of C/C_0 after irradiation of 60 minutes, implying that incomplete mineralization of TC and formation of some organic compounds with small molecule weight.

3.3 Photocatalytic Mechanism

In order to find out the active radicals in the photocatalytic degradation, the free radical capture experiments were conducted. Isopropyl

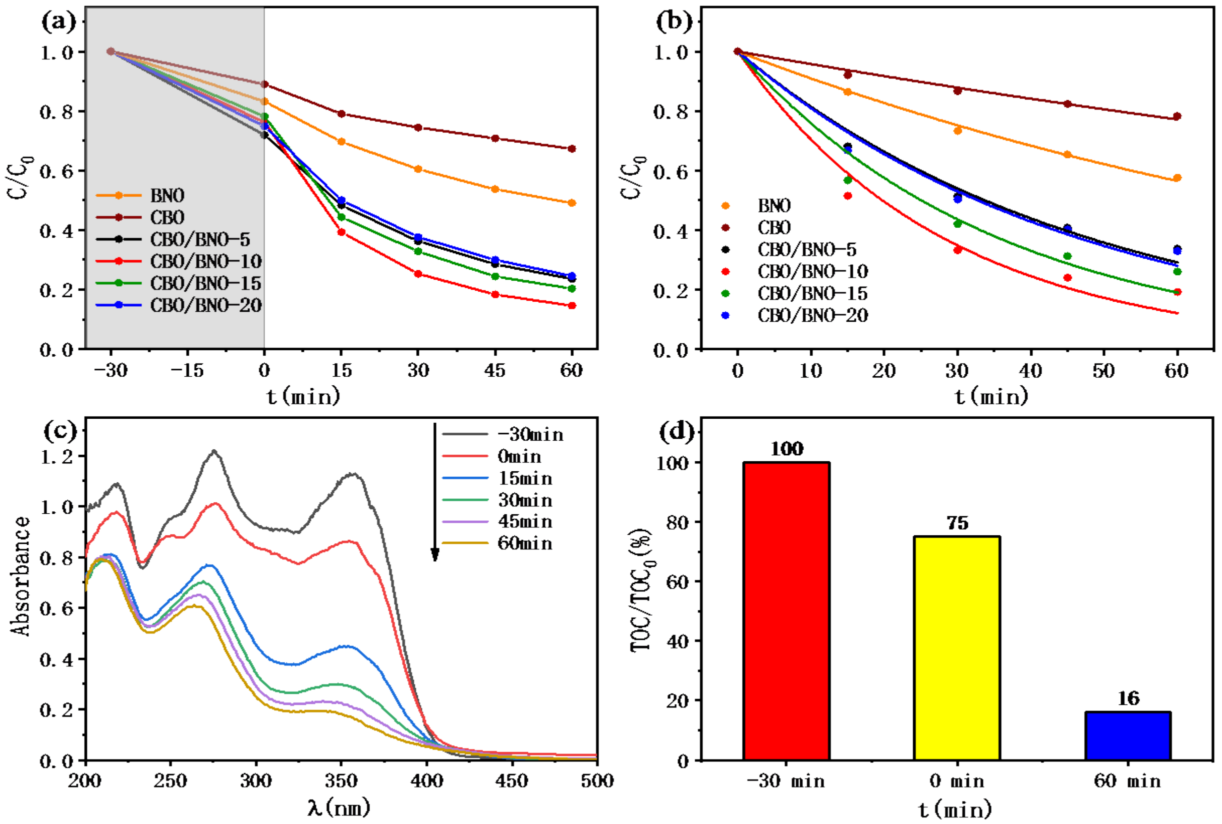

Figure 8. (a) Photocatalytic degradation efficiency of TC on CBO, BNO and CBO/BNO composites; (b) first-order kinetics fitting plots; (c) UV-vis scanning curves of solutions during photocatalytic process; (d) results of TOC analysis.

alcohol (IPA), potassium iodide (KI) and *p*-benzoquinone (BQ), were used as quenching agents for the hydroxyl radical ($\cdot OH$), the photogenic hole (h^+) and the superoxide radical ($\cdot O_2^-$), respectively. As illustrated in Figure 9a, the TC degradation efficiency decreased by the introductions of the above capture agents, suggesting that the active radicals $\cdot O_2^-$ and h^+ take part in the TC degradation in the order of $\cdot O_2^- > h^+$, except $\cdot OH$. To further verify the roles of active radicals, EPR tests were carried out. The EPR results indicate that the intensive signals of $\cdot O_2^-$ and h^+ presented under irradiation of light, while no distinct $\cdot OH$ signal was detected. The EPR results are consistent with those of active radicals capture experiments.

Based on the above results, we proposed the type-II mechanism for photocatalytic degradation of TC on the CBO/BNO heterojunction photocatalyst. CBO and BNO are *p*-type and *n*-type semiconductors, respectively, when they contact with each other, a *p-n* heterojunction is formed. As a result, an internal electric field (IEF) from BNO to CBO is built at their interface. XPS results (Figure 5) revealed that electrons flowed from BNO to CBO after the CBO/BNO heterojunction was constructed. Under irradiation of stimulated sunlight, electrons and holes were excited on CBO and BNO, respectively. The photo-excited electrons (e^-) on the CB of BNO moved to CB of CBO, while photo-excited holes (h^+) moved from VB of BNO to VB of CBO. The e^- on the CB of Bi_3NbO_7 reduced O_2 into superoxide radical ($\cdot O_2^-$) anions, due to its potential is more negative than that of $O_2/\cdot O_2^-$ (−0.33 eV *vs* NHE). However, the h^+ on VB of CBO can degrade the TC molecules directly. Moreover, because the potential of photo-excited holes on VB of CBO was lower than the standard redox potentials of $\cdot OH/OH^-$ (1.99 eV *vs* NHE) and $\cdot OH/H_2O$ (+2.72 eV *vs* NHE), no $\cdot OH$ was produced, as observed in the results of active radicals capture experiments. The photocatalytic degradation mechanism is illustrated in Figure 10.

3.4 Reusability

The usability of the CBO/BNO heterojunction was studied by the cycle use experiment. As shown in Figure 11, the TC degradation efficiency decreased from 85% to 74% after five cycles of use, indicating the CBO/BNO heterojunction has better usability. In order to investigate the changes in structure and physical properties, the used photocatalyst were characterized by XRD, BET, SEM and XPS. XRD result (Figure 11b) shows that there is no change in the positions of diffraction peaks, compared with the fresh photocatalyst, illustrating the crystal structure was kept after use. However, the specific surface area (Table S1) decreased slightly, originated from the loss in the amounts of active sites. As shown in Figure S3, compared with the fresh

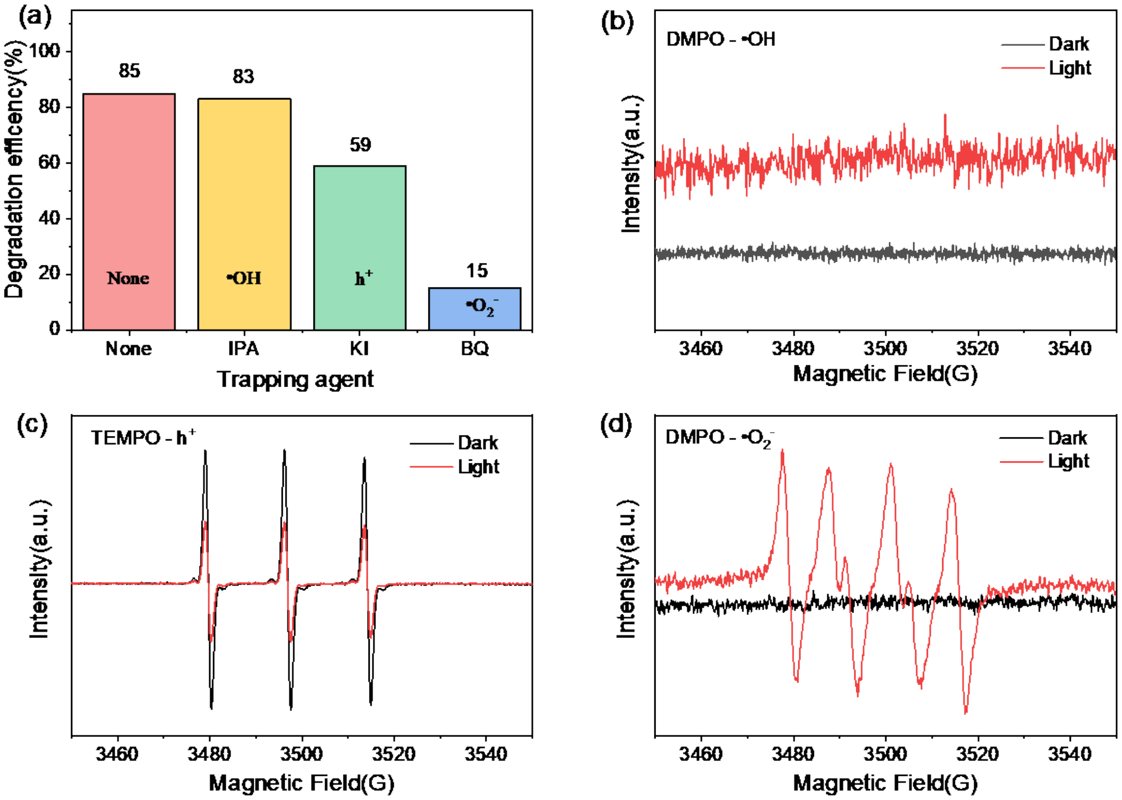

Figure 9. (a) Free active radicals capture experiments and EPR spectra of (b) h^+, (c) $\cdot O_2^-$, (d) $\cdot OH$.

photocatalyst, the C 1s spectrum of used photocatalyst displays relative intensive peaks which are associated to C-O and C=O, illustrating that the existence of organic compounds on the photocatalyst surface. In summary, the loss in photocatalytic activity is because of the adsorption of intermediates or undegraded TC molecules on the surface of photocatalyst, occupying the active sites and blocking the pores of the photocatalyst.

4. Conclusion

The $CuBi_2O_4/Bi_3NbO_7$ heterojunction was successfully prepared. This heterojunction greatly improved the photocatalytic activity of Bi_3NbO_7 under stimulated sunlight irradiation, owing to the effective separation of photo-excited electrons and holes. The optimal TC degradation efficiency of 85% was obtained on sample CBO/BNO-10 at the condition as initial TC concentration of 40 mg/L and photocatalyst dosage of 1 g/L, and its reaction rate constant reached 0.035 min^{-1}, which is 3.7 times as that of Bi_3NbO_7. The $CuBi_2O_4/Bi_3NbO_7$ exhibited better reusability that TC degradation efficiency of 74% was obtained after five cycles of use. This work provided a method for improving the photocatalytic activity of Bi_3NbO_7 photocatalyst and may be applied to the wastewater treatment processes after further investigations in feasibility to industrial application.

Acknowledgment

The authors would like to thank Shenyang University of Chemical Technology for all the support received and for allowing the publishing of this work.

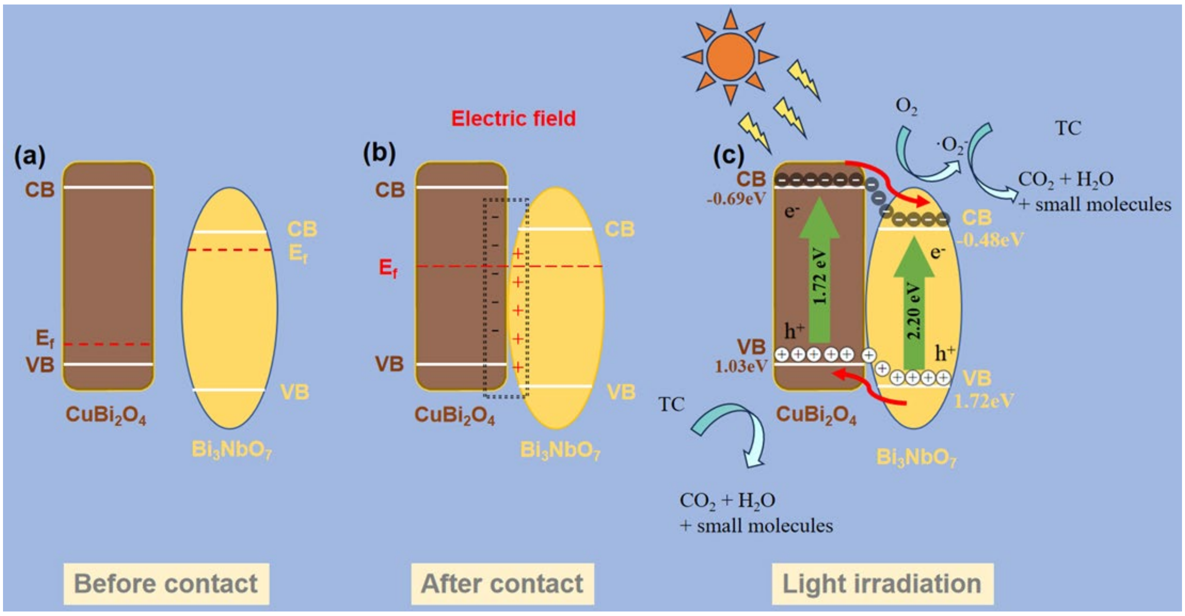

Figure 10. Schematic diagram of photocatalytic degradation mechanism.

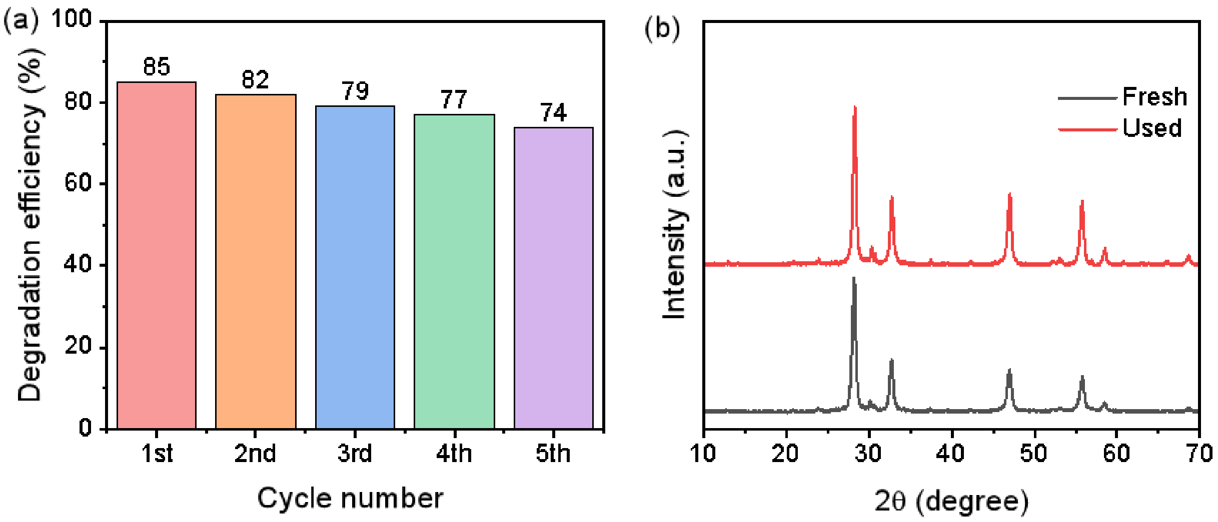

Figure 11. (a) Results of reusability tests and (b) XRD patterns of CBO/BNO-10 before and after use.

CRedit Author Statement

Author Contributions: Zhenkun Cheng: Writing – review & editing, Writing – original draft, Investigation, Data curation. Dongbin Liu: Methodology, Investigation, Data curation. Lihui Fan: Methodology, Investigation, Data curation. Yanming Shen: Writing – review & editing, Writing – original draft, Conceptualization. All authors have read and agreed to the published version of the manuscript.

References

[1] Wang, H., Zhang, S., Lin, Z., Xiao, F., Xiang, B., Li, A. (2025). Occurrence, removal and ecological risk assessment of antibiotics in rural domestic wastewater treatment systems in the Beijing-Tianjin-Hebei region. *Journal of Hazardous Materials*, 495, 139127. DOI: 10.1016/j.jhazmat.2025.139127.

[2] Srivastava, S.K. (2024). Recent advances in removal of pharmaceutical pollutants in wastewater using metal oxides and carbonaceous materials as photocatalysts: a review. *RSC Applied Interfaces*, 1(3), 340-429. DOI: 10.1039/D3LF00142C.

[3] Venkatesan, L.S., Sathishkumar, P. (2025). Recent advances in the removal of emerging pollutant tetracycline using green nanomaterials: An eco-friendly mitigation approach. *International Journal of Environmental Science and Technology*, 22(6), 5129-5142. DOI: 10.1007/s13762-024-06163-w.

[4] Scaria, J., Anupama, K.V., Nidheesh, P.V. (2021). Tetracyclines in the environment: An overview on the occurrence, fate, toxicity, detection, removal methods, and sludge management. *Science of the Total Environment*, 771, 145291. DOI: 10.1016/j.scitotenv.2021.145291.

[5] Zhang, X., Cai, T., Zhang, S., Hou, J., Cheng, L., Chen, W., Zhang, Q. (2024). Contamination distribution and non-biological removal pathways of typical tetracycline antibiotics in the environment: A review. *Journal of Hazardous Materials*, 463, 132862. DOI: 10.1016/j.jhazmat.2023.132862.

[6] Gopal, G., Alex, S.A., Chandrasekaran, N., Mukherjee, A. (2020). A review on tetracycline removal from aqueous systems by advanced treatment techniques. *RSC Advances*, 10(45), 27081-27095. DOI: 10.1039/D0RA04264A.

[7] Singh, P.P., Pandey, G., Murti, Y., Gairola, J., Mahajan, S., Kandhari, H., Tivari, S., Srivastava, V. (2024). Light-driven photocatalysis as an effective tool for degradation of antibiotics. *RSC Advances*, 14(29), 20492-20515. DOI: 10.1039/D4RA03431G.

[8] Rab, S.O., Altalbawy, F.M.A., Baldaniya, L., Kumar, A., M M, R., Kundlas, M., Sharma, G.C., Joshi, K.K., Saydaxmetova, S., Abosaoda, M.K. (2025). A comprehensive review of bismuth-based photocatalysts and antibiotic pollution degradation: Recent trends and challenges. *Inorganic Chemistry Communications*, 174, 114067. DOI: 10.1016/j.inoche.2025.114067.

[9] Mane, V., Dake, D., Raskar, N., Sonpir, R., Stathatos, E., Dole, B. (2024). A review on Bi2O3 nanomaterial for photocatalytic and antibacterial applications. *Chemical Physics Impact*, 8, 100517. DOI: 10.1016/j.chphi.2024.100517.

[10] Chen, L., Xu, B., Jin, M., Chen, L., Yi, G., Xing, B., Zhang, Y., Wu, Y., Li, Z. (2023). Excellent photocatalysis of Bi_2WO_6 structured with oxygen vacancies in degradation of tetracycline. *Journal of Molecular Structure*, 1278, 134911. DOI: 10.1016/j.molstruc.2023.134911.

[11] Thakur, V., Singh, S., Kumar, P., Rawat, S., Chandra Srivastava, V., Lo, S.-L., Lavrenčič Štangar, U. (2023). Photocatalytic behaviors of bismuth-based mixed oxides: Types, fabrication techniques and mineralization mechanism of antibiotics. *Chemical Engineering Journal*, 475, 146100. DOI: 10.1016/j.cej.2023.146100.

[12] Bulut, D.T. (2025). Exploring the dual role of $BiVO_4$ nanoparticles: unveiling enhanced antimicrobial efficacy and photocatalytic performance. *Journal of Sol-Gel Science and Technology*, 114(1), 198-222. DOI: 10.1007/s10971-025-06682-z.

[13] Wang, Q., Yuan, L., Dun, M., Yang, X., Chen, H., Li, J., Hu, J. (2016). Synthesis and characterization of visible light responsive Bi_3NbO_7 porous nanosheets photocatalyst. *Applied Catalysis B: Environmental*, 196, 127-134. DOI: 10.1016/j.apcatb.2016.05.026.

[14] Wang, S., Wang, L., Huang, W. (2020). Bismuth-based photocatalysts for solar energy conversion. *Journal of Materials Chemistry A*, 8(46), 24307-24352. DOI: 10.1039/D0TA09729B.

[15] Yayuk Astuti, A.M., Adi Darmawan. (2026). Tailoring Photocatalytic Activity of Sol-Gel-Derived Bismuth Oxide via Calcination Time Optimization for Methyl Orange Degradation. *Bulletin of Chemical Reaction Engineering & Catalysis*, 21(1), 11-21. DOI: 10.9767/bcrec.20452.

[16] Li, R., Chen, H., Xiong, J., Xu, X., Cheng, J., Liu, X., Liu, G. (2020). A Mini Review on Bismuth-Based Z-Scheme Photocatalysts. *Materials*, 13(22), 5057. DOI: 10.3390/ma13225057.

[17] Vadivel, S., Paul, B., Saravanakumar, B., Periasamy, P.A. (2024). Facile synthesis of bismuth niobium oxide (Bi_3NbO_7) micro squares as a novel pseudocapacitive electrode material for supercapacitors. *Materials Letters*, 363, 136295. DOI: 10.1016/j.matlet.2024.136295.

[18] Ai, Z., Ho, W., Lee, S. (2012). A stable single-crystal Bi3NbO7 nanoplates superstructure for effective visible-light-driven photocatalytic removal of nitric oxide. *Applied Surface Science*, 263, 266-272. DOI: 10.1016/j.apsusc.2012.09.041.

[19] Fang, J., Ma, J., Sun, Y., Liu, Z., Gao, C. (2011). Synthesis of Bi_3NbO_7 nanoparticles with a hollow structure and their photocatalytic activity under visible light. *Solid State Sciences*, 13(8), 1649-1653. DOI: 10.1016/j.solidstatesciences.2011.06.017.

[20] Zhang, G., Yang, J., Zhang, S., Xiong, Q., Huang, B., Wang, J., Gong, W. (2009). Preparation of nanosized Bi_3NbO_7 and its visible-light photocatalytic property. *Journal of Hazardous Materials*, 172(2), 986-992. DOI: 10.1016/j.jhazmat.2009.07.089.

[21] Tian, Z., Guo, Y., Wang, M., Li, Y., Zhao, S. (2025). Facile synthesis of porous tubular Bi_3NbO_7 electrocatalyst for the simultaneous determination of antihypertensive drugs amlodipine and hydrochlorothiazide. *Microchemical Journal*, 216, 114634. DOI: 10.1016/j.microc.2025.114634.

[22] Graimed, B.H., Jabbar, Z.H., Alsunbuli, M.M., Ammar, S.H., G. Taher, A. (2024). Decoration of 0D Bi_3NbO_7 nanoparticles onto 2D $BiOIO_3$ nanosheets as visible-light responsive S-scheme photocatalyst for photo-oxidation of antibiotics in wastewater. *Environmental Research*, 243, 117854. DOI: 10.1016/j.envres.2023.117854.

[23] Cui, B., Xue, H., Pan, Y., Du, Y. (2024). S-Scheme Nanometer-Sized $Bi_3NbO_7/Bi_2O_2CO_3$ Heterojunction Photocatalysts for Efficient Pollutant Degradation. *ACS Applied Nano Materials*, 7(13), 15547-15556. DOI: 10.1021/acsanm.4c02457.

[24] Yang, L., Shen, Y., Dou, Y., Wen, J. (2025). Combination of CuO with Bi_3NbO_7 for Boosting Photocatalytic Performance Under Visible Light. *Korean Journal of Chemical Engineering*, 42(10), 2309-2319. DOI: 10.1007/s11814-025-00463-8.

[25] Cui, B., Leng, W., Wang, X., Wang, Y., Wang, J., Hu, Y., Du, Y. (2023). Enhanced visible-light photocatalytic activity of S-scheme Bi_3NbO_7/Bi_2MoO_6 heterojunction composite photocatalyst. *Vacuum*, 217, 112589. DOI: 10.1016/j.vacuum.2023.112589.

[26] Sun, X., Shi, L., Bai, Q., Yin, Z., Song, H., Qu, X. (2022). Synthesis of $BiOCl/Bi_3NbO_7$ heterojunction by in-situ chemical etching with enhanced photocatalytic performance for the degradation of organic pollutants. *Applied Surface Science*, 587, 152633. DOI: 10.1016/j.apsusc.2022.152633.

[27] Ren, Y., Gong, T., Tan, S., Chen, M., Zhou, F., Lin, Y., Yang, L., Peng, Q. (2022). Photocatalytic activities of g-C_3N_4, Bi_3NbO_7 and g-C_3N_4/Bi_3NbO_7 in photocatalytic reduction of Cr(VI). *Journal of Alloys and Compounds*, 902, 163752. DOI: 10.1016/j.jallcom.2022.163752.

[28] Liu, Y., Xu, J., Chen, M. (2021). Synthesis of direct Z-Scheme $Bi_3NbO_7/BiOCl$ photocatalysts with enhanced activity for CIP degradation and Cr(VI) reduction under visible light irradiation. *Separation and Purification Technology*, 276, 119255. DOI: 10.1016/j.seppur.2021.119255.

[29] Xu, J., Liu, C., Niu, J., Zhu, Y., Zang, B., Xie, M., Chen, M. (2020). Synthesis of $LaFeO_3/Bi_3NbO_7$ p-n heterojunction photocatalysts with enhanced visible-light-responsive activity for photocatalytic reduction of Cr(VI). *Journal of Alloys and Compounds*, 815, 152492. DOI: 10.1016/j.jallcom.2019.152492.

[30] Hou, J., Wang, Z., Jiao, S., Zhu, H. (2012). Bi2O3 quantum-dot decorated nitrogen-doped Bi_3NbO_7 nanosheets: in situ synthesis and enhanced visible-light photocatalytic activity. *CrystEngComm*, 14(18), 5923-5928. DOI: 10.1039/C2CE25504A.

[31] Olatunde, O.C., Sawunyama, L., Yusuf, T.L., Onwudiwe, D.C. (2024). Visible light driven $CuBi_2O_4$ heterostructures and their enhanced photocatalytic activity for pollutant degradation: A review. *Journal of Water Process Engineering*, 66, 105890. DOI: 10.1016/j.jwpe.2024.105890.

[32] Jabbar, Z.H., Graimed, B.H., Ammar, S.H., Taher, A.G., Majdi, A., Mohammed, A.A. (2024). The latest innovations in $CuBi_2O_4$-based photocatalysts and their contribution in degradation of toxic organic pollutants under simulated solar energy. *Solar Energy*, 282, 112988. DOI: 10.1016/j.solener.2024.112988.

[33] Tarannum, T., Soni, V., Singh, P., Ahamad, T., Van Le, Q., Nguyen, V.-H., Thakur, S., Raizada, P. (2026). Design principles and mechanistic strategies of $CuBi_2O_4$-based S-scheme catalytic systems for environmental photocatalysis. *Inorganic Chemistry Communications*, 183, 115884. DOI: 10.1016/j.inoche.2025.115884.

[34] Li, J., Fan, L., Liu, D., Shen, Y. Photocatalytic degradation of tetracycline by WO_3/Bi_3NbO_7 S-scheme heterojunction photocatalyst. *Journal of the Chinese Chemical Society*, DOI: 10.1002/jccs.70162.

[35] Nogueira, A.C., Gomes, L.E., Ferencz, J.A.P., Rodrigues, J.E.F.S., Gonçalves, R.V., Wender, H. (2019). Improved Visible Light Photoactivity of $CuBi_2O_4/CuO$ Heterojunctions for Photodegradation of Methylene Blue and Metronidazole. *The Journal of Physical Chemistry C*, 123(42), 25680-25690. DOI: 10.1021/acs.jpcc.9b06907.

[36] Liu, Y., Han, Y., Qiu, H., Yang, M., Zhang, M., Wang, Y., Xiang, Z., Liu, W., Wang, X. (2025). Construction of $Ag_2WO_4/CuBi_2O_4$ S-Scheme Heterojunctions with Enhanced Sonocatalytic Performance for the Removal of Tetracycline: Characterization, Sonocatalytic Mechanism, and Degradation Pathways. *Langmuir*, 41(22), 13916-13931. DOI: 10.1021/acs.langmuir.5c00744.

[37] Ashfaq, M., Talreja, N., Chauhan, D., Rodríguez, C.A., Mera, A.C., Viswanathan, M.R. (2022). A facile synthesis of $CuBi_2O_4$ hierarchical dumbbell-shaped nanorod cluster: a promising photocatalyst for the degradation of caffeic acid. *Environmental Science and Pollution Research*, 29(35), 53873-53883. DOI: 10.1007/s11356-022-19592-2.

[38] Mondal, S., Patra, L., Ilanchezhiyan, P., Neppolian, B., Pandey, R., Ganesh, V. (2024). In Situ Growth of $CuBi_2O_4/Bi_2O_3$ Z-Scheme Heterostructures for Bifunctional Photocatalytic Applications. *Langmuir*, 40(25), 12954-12966. DOI: 10.1021/acs.langmuir.4c00589.

[39] Zhang, C., Liu, F., He, Q., Li, J., Jiang, W., Zhan, S., Zhou, F. (2024). Enhanced Fenton-like catalysis through in-situ bismuth defection in $Bi/CuBi_2O_4$: Vacancy mechanisms. *Journal of Environmental Chemical Engineering*, 12(3), 112511. DOI: 10.1016/j.jece.2024.112511.

[40] Huang, R., Liu, X., Yang, X., Rao, Z., Cai, W., Wang, Z., Gao, R., Chen, G., Deng, X., Lei, X., Fu, C. (2023). Piezo-Phototronic Coupling Effect in $CuBi_2O_4/AgNbO_3$ Z-Scheme Heterojunction for High-Efficiency Decomposition of Organic Dye. *ACS Applied Electronic Materials*, 5(11), 6197-6211. DOI: 10.1021/acsaelm.3c01109.

[41] Brik, A., Hadjersi, T., Khaled, D., Naama, S., Bendadel, K., Souraya, B., Benredouane, S., Khadija, B. (2025). Tetracycline Degradation Under Visible Light Using a New $SiNW/CeO_2/NiO$ Composite as a High-Efficiency Photocatalyst. *Journal of Inorganic and Organometallic Polymers and Materials*, 35(12), 10029-10042. DOI: 10.1007/s10904-025-03888-0.